

WHY ARE SOME GALAXIES NOT BARRED?

KANAK SAHA¹ & BRUCE ELMEGREEN²

¹ Inter-University Centre for Astronomy and Astrophysics, Pune 411007, India,

² IBM Research Division, T. J. Watson Research Center, 1101 Kitchawan Road, Yorktown Heights, NY 10598, USA
e-mail: kanak@iucaa.in, bge@us.ibm.com

Draft version March 29, 2018

ABSTRACT

Although more than two-thirds of star-forming disk galaxies in the local universe are barred, some galaxies remain un-barred, occupying the upper half of the Hubble tuning fork diagram. Numerical simulations almost always produce bars spontaneously, so it remains a challenge to understand how galaxies sometimes prevent bars from forming. Using a set of collisionless simulations, we first reproduce the common result that cold stellar disks surrounding a classical bulge become strongly unstable to non-axisymmetric perturbations, leading to the rapid formation of spiral structure and bars. However, our analyses show that galaxy models with compact classical bulges (whose average density is greater than or comparable to the disk density calculated within bulge half-mass radii) are able to prevent bar formation for at least 4 Gyr even when the stellar disk is maximal and having low Toomre Q . Such bar prevention is the result of several factors such as (a) a small inner Lindblad resonance with a high angular rate, which contaminates an incipient bar with x_2 orbits, (b) rapid loss of angular momentum accompanied by a rapid heating in the center from initially strong bar and spiral instabilities in a low- Q disk, in other words, a rapid initial rise to a value larger than ~ 5 of the ratio of the random energy to the rotational energy in the central region of the galaxy.

Subject headings: galaxies:bulges – galaxies:kinematics and dynamics – galaxies:structure – galaxies:evolution – galaxies:spiral, galaxies:halos

1. INTRODUCTION

Stellar bars are one of the most common non-axisymmetric structures in spiral galaxies. More than 60% of disk galaxies in the local universe are strongly barred (Eskridge et al. 2000; Grosbøl et al. 2004; Menéndez-Delmestre et al. 2007; Barazza et al. 2008). Our local group is no exception to this. Bars are also seen out to redshifts $z \sim 1$ (Sheth et al. 2008), corresponding to 8 Gyr ago, which implies that once formed, a bar is hard to destroy (Athanassoula et al. 2005). Bars also seem to have formed relatively quickly, as they appeared soon after galaxy disks became cool (Sheth et al. 2012). Thus it remains unclear why all galaxies are not barred.

Most of our knowledge about bar formation has come from numerical simulations, starting with Miller et al. (1970) and Hohl (1971). Simulations of isolated galaxies with cool stellar disks show the spontaneous formation of bars from gravitationally unstable $m = 2$ modes (Toomre 1964; Goldreich & Tremaine 1979; Toomre 1981; Combes & Sanders 1981; Sellwood & Wilkinson 1993; Polyachenko 2013), or from galaxy interactions and mergers (Noguchi 1987; Gerin et al. 1990; Elmegreen et al. 1991; Barnes & Hernquist 1991; Miwa & Noguchi 1998) or interactions with dark matter halo substructures (Romano-Díaz et al. 2008). Resonant gravitational interactions that transfer disk angular momentum to the dark matter halo lead to long-term bar stability and growth (Debattista & Sellwood 1998; Athanassoula & Misiriotis 2002; Athanassoula 2003; Holley-Bockelmann et al. 2005; Weinberg & Katz 2007a; Ceverino & Klypin 2007; Dubinski et al. 2009; Saha et al. 2012). Even hot stellar disks that are otherwise stable can form bars if they are embedded in a

spinning dark matter halo (Saha & Naab 2013).

There have been a number of studies that addressed this issue by finding processes that can destroy a bar. The usual suspects are central mass concentrations (CMC) and super-massive black holes (SMBHs), possible fed by gas inflow (Bournaud & Combes 2002). Both CMCs and SMBHs can affect the orbital distribution of stars in a bar and dissolve the bar on timescales of a few Gyr or less (Pfenniger & Norman 1990; Hasan et al. 1993; Hozumi & Hernquist 2005). However, other studies suggest that bars are difficult to destroy because the central mass has to be unreasonably large, such as $\sim 10\%$ of the disk mass (Shen & Sellwood 2004; Athanassoula et al. 2005). Also, CMCs and SMBHs are present in barred galaxies, so they seem to co-exist. What has yet to be determined is whether a bar can grow in the first place in the presence of such compact objects. Perhaps the prevention of bar formation at an early stage is easier than the destruction of the bar after it gets massive.

The present paper uses self-consistent simulations that probe the impact of compact classical bulges on bar growth. Sec 2 describes the simulated galaxies and Sec 3 discusses bar formation and various early effects introduced by a bulge. Sec 4 investigates in detail, the dynamics and evolution of two models. The discussion and conclusions are in Sec 5.

2. GALAXY MODEL AND SIMULATION

We construct a set of 15 three-component galaxy models consisting of a stellar disk, a dark matter halo, and a classical bulge, initially in equilibrium. The stellar disk is initially axisymmetric with surface density following an exponential profile with scale length R_d and central

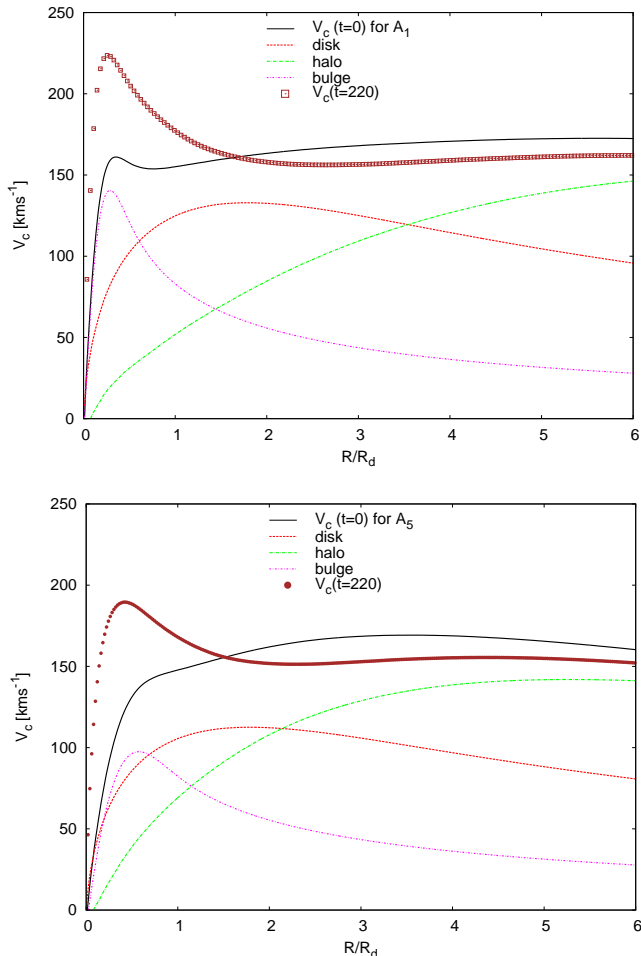


FIG. 1.— Circular Velocity curves for model A_1 (upper) and A_5 (lower). Time is in internal unit.

surface density Σ_0 . The initial vertical scale height is kept constant for simplicity and follows a $sech^2$ distribution, with scale-height $h_z = 0.02R_d$ for all models. For self-consistency, we let the vertical velocity dispersion follow also an exponential profile with a scale length equal to twice that of the surface density. The dark matter halo is modelled with a lowered Evans (1993) model, which produces a nearly flat circular velocity profile, see Fig. 1 for two models, A_1 and A_5 . The bulge is modelled with a King distribution function (DF, King 1966) and their properties are discussed below. Further details about the distribution function and model construction can be found in Kuijken & Dubinski (1995) and Saha et al. (2012). The dark matter halo mass is kept nearly constant in most models at about $M_h \simeq 4M_d$; slight variations are reported in Table 1. The stellar disk is the same in all models. The mass and size of the initial classical bulge vary the most from model to model.

2.1. Properties of model classical bulges

A spherical live classical bulge (hereafter CIBs) is constructed from the King model. For the sake of completeness, the corresponding DF is given by (Kuijken & Dubinski 1995)

$$f_b(E) = \begin{cases} \rho_b(2\pi\sigma_b^2)^{-3/2}e^{(\Psi_{b0}-\Psi_c)/\sigma_b^2} \\ \times \{e^{-(E-\Psi_c)/\sigma_b^2} - 1\} & \text{if } E < \Psi_c, \\ 0 & \text{otherwise.} \end{cases} \quad (1)$$

Here, the bulge is specified by three parameters, namely the cut-off potential (Ψ_c) which determines the bulge tidal radius, central bulge density (ρ_b) and central bulge velocity dispersion (σ_b). The gravitational potential at the centre of the bulge is measured by Ψ_{b0} . The radial density profile has a core at the centre and sharply drops to zero at the tidal radius. The more negative the Ψ_c , the more centrally concentrated and radially confined is the bulge. The parameters σ_b and ρ_b control the mass and size of the bulge. Initially, we picked a range of values for these parameters, namely $\rho_b = 3.4 - 250.8$, $\sigma_b = 0.7 - 2.5$. The value of Ψ_c was varied the least, from -2.8 to -3.2 . Most of B-series models (see below) had higher ρ_b and Ψ_c , e.g., for the B_1 model they are 250.8 and -3.2 respectively. Note that there is no one-to-one correspondence between these parameters of the DF and the mass model of the bulge (e.g., bulge mass and tidal radius), since the bulge is gravitationally coupled with the other two components, disk and halo. Not all sets of parameters lead to convergence when creating a galaxy model, see (Kuijken & Dubinski 1995) and its user manual for GalactICs.

In the left panel of Fig. 2, we show the relation between the bulge size (measured by R_{half} , the bulge half-mass radii) and the bulge-to-total (B/T) ratio for each galaxy model, where B denotes the bulge mass and T denotes the total stellar mass for our simulated galaxy models. To these simulated CIBs, we fit the following linear regression model between $\log[R_{half}]$ and $\log[B/T]$:

$$R_{half}/R_d = C_0(B/T)^\alpha, \quad (2)$$

where C_0 is a constant and α is the power-law exponent. Fig. 2 shows two tracks for the distribution of the bulge size with the B/T ratio. We call these type A and B models, with type A representing the less compact bulges and type B representing the more compact bulges.

TABLE 1
INITIAL PARAMETERS OF THE GALAXY MODELS.

Models	M_h/M_d	B/T	R_{half}/R_d	$Q_{2.5}$	ρ_{bulge}	ρ_{disk}
A_1	4.3	0.114	0.18	1.208	4.88	14.1
A_2	4.2	0.121	0.20	1.280	3.63	13.9
A_3	4.2	0.128	0.23	1.300	2.65	13.6
A_4	4.1	0.137	0.28	1.335	1.72	13.2
A_5	4.0	0.148	0.37	1.437	0.80	12.5
B_1	4.5	0.07	0.07	0.953	53.7	15.2
B_2	4.2	0.10	0.10	1.043	21.0	14.9
B_3	4.3	0.121	0.144	1.099	10.8	14.4
B_4	4.2	0.128	0.147	1.107	10.7	14.4
B_5	4.0	0.18	0.25	1.097	3.2	13.5
B_6	4.0	0.20	0.29	1.136	2.4	13.1
B_7	3.5	0.23	0.33	1.185	1.92	12.8
B_8	4.2	0.24	0.35	1.154	1.72	12.6
B_9	3.5	0.25	0.37	1.164	1.50	12.5
B_{10}	4.1	0.27	0.50	1.198	0.69	11.5

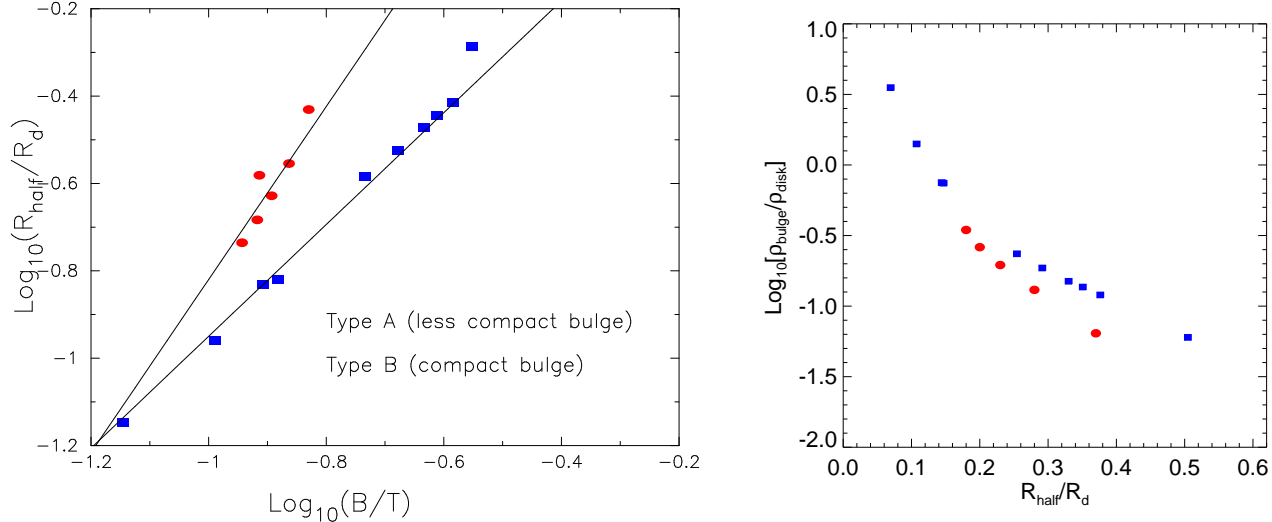


FIG. 2.— Left: Mass-size relation for two different sets of classical bulges, type A and type B. For a given B/T , type B bulges are more compact than type A. Right: Bulge density normalized by the disk density within R_{half} plotted against their half-mass radii. Two bulges from type B have densities higher than their respective disk density (see table 1).

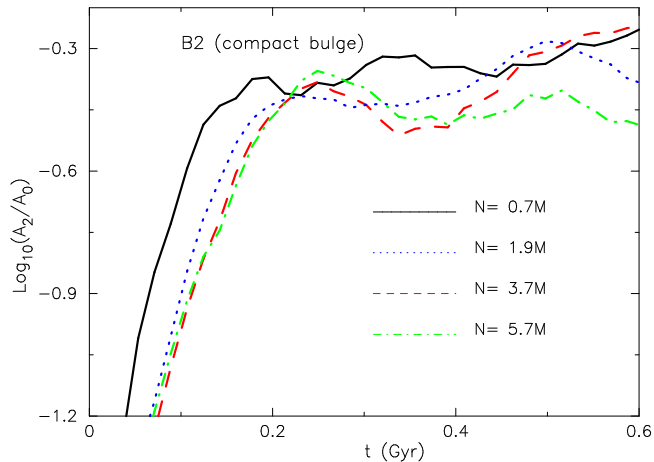


FIG. 3.— Time evolution of the A_2/A_0 for model B_2 and dependence on the number of particles used in the simulation.

For type A ClBs, we have $\alpha = 1.98$ and $C_0 = 1.16$. For type B ClBs, they are 1.28 and 0.33 respectively. A similar relation holds for the outer radii (R_b) of the King bulges and B/T , with $\alpha = 2.0$, $C_0 = 1.73$ for type A ClBs. For type B, they are 1.2 and 0.85 respectively. So for a given B/T , type B bulges are more compact than type A bulges. On the right panel of Fig. 2, we show the dependence of the average bulge density on the half-mass radius. The bulge density is computed as $\rho_{bulge} = 3M_{b,1/2}/(4\pi R_{half}^3)$, where $M_{b,1/2}$ is the ClB mass within R_{half} . These quantities are calculated exclusively using the bulge particles (following their unique id's in the simulation). We normalize the bulge density with the density of disk stars (ρ_{disk}) measured within R_{half} , see Table 1. This ratio is given by:

$$\frac{\rho_{bulge}}{\rho_{disk}} = \frac{M_{b,1/2}}{M_d} \frac{3h_z}{4R_{half}} [1 - e^{-R_{half}/R_d} \times (1 + R_{half}/R_d)]^{-1}, \quad (3)$$

The right panel of Fig. 2 demonstrates that type A

bulges are less dense compared to type B. In other words, we can say that type B bulges are more compact and dense than type A.

We scale the models such that $R_d = 3$ kpc and the circular velocity at $2R_d$ is 160 km/s. The unit of time varies from model to model as the bulge mass varies. We have used a total of 3.7×10^6 particles, with 2.0×10^6 for the dark matter halo, 1.2×10^6 for the disk and 0.5×10^6 for the bulge particles. The softening lengths for the disk, bulge and halo particles are calculated following the suggestion of McMillan & Dehnen (2007). The simulation is performed using the Gadget-1 code (Springel et al. 2001), which uses the quadrupole contribution to the force calculation, using a tolerance parameter $\theta_{tol} = 0.7$ and an integration time step of 0.03 times the internal time unit. The simulation was evolved for a time period of ~ 4.0 Gyr. The energy is conserved within 0.1% and angular momentum within 1% for entire duration of the run.

We have also run a few more simulations to check convergence with respect to the number of particles. In particular, we have re-run model B_2 which evolved into an unbarred galaxy, with particle numbers varying from 0.7 million to 5.7 million. We noticed that increasing particle number delays the linear growth as expected; we found ~ 50 Myr of delay as the particle number was increased by a factor of 8. Fig. 3 demonstrates that the linear growth phase remains nearly same between $N = 3.7$ and 5.7 million particles. The convergence on the number of particles in our simulation is in compliance with previous results found in Dubinski et al. (2009) and Saha et al. (2010). We also noticed that model B_2 evolved always into an unbarred case irrespective of the particle number, provided it was about a few million.

3. FORMATION OF STELLAR BARS

The stellar disks in all of the models are cold with Q varying from $\sim 0.95 - 1.4$ to begin with; see table 1. The radial profiles of $Q(R)$ are shown in the upper panels of Fig. 4 for type A and type B models. Being in the cold regime, the stellar disks in all models become gravita-

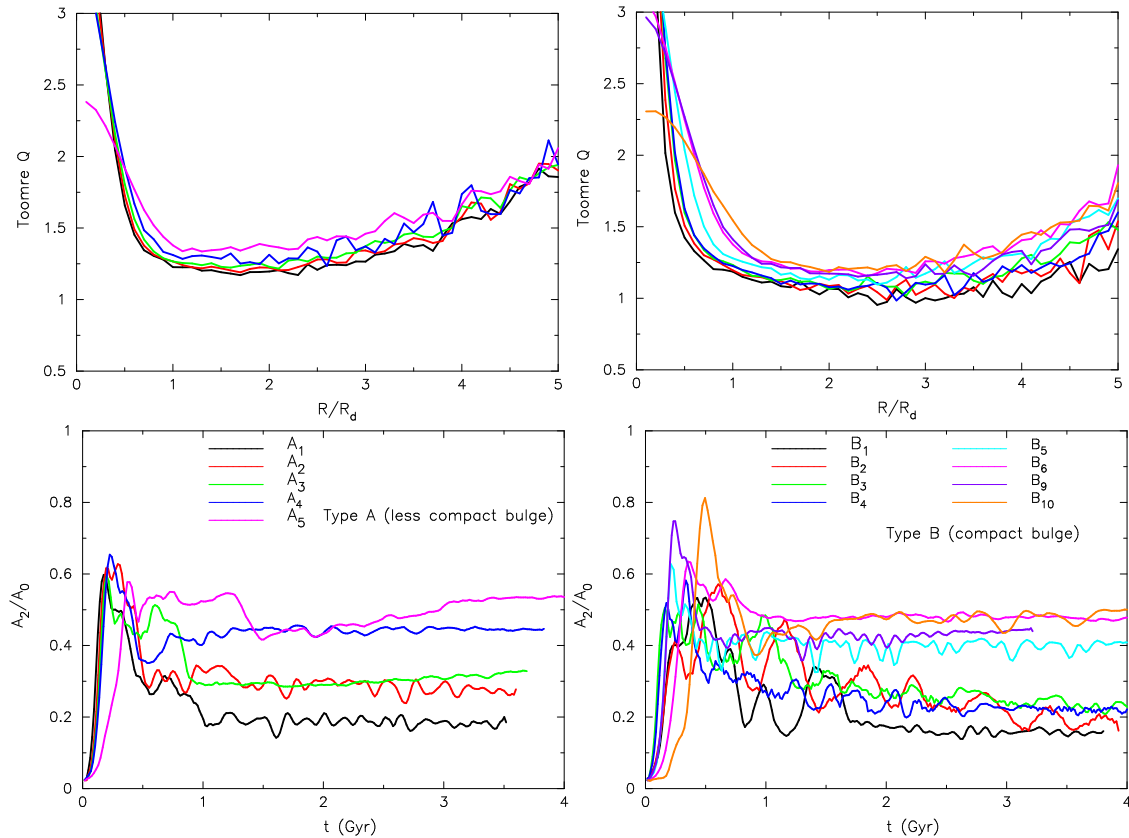


FIG. 4.— Left panels: initial radial profile of Toomre Q (upper) and time evolution of A_2/A_0 (lower) for type A models. Right panels: same as left panels but for type B.

tionally unstable and form wide-open spiral arms within a few rotation times. The lower panels of Fig. 4 show the time evolution of the peak of the $m = 2$ Fourier component (A_2) normalized by the $m = 0$ Fourier component (A_0). The value of A_2/A_0 sharply rises to ~ 0.6 within ~ 0.5 Gyr for all models irrespective of the ClBs they host. As long as the stellar disk is cold, the morphological evolution in the initial stage is nearly the same and is determined by the initial Toomre Q . The spiral arms grow stronger in the first ~ 0.5 Gyr, at which time their amplitude growth saturates and fragment into clumps due to non-linear effects. These spiral arms also contribute to disk heating while dissolving (Saha et al. 2010). Stellar clumps that result from the fragmented spirals migrate to the central region and contribute to the growth of the pre-existing ClB. This can be visualized through the sequence of images presented in Fig. 5 for type A models. At about 0.5 Gyr or before, all five type A models have similar morphology, as determined primarily by the disk Q value.

Small differences in the initial growth rate of the $m = 2$ component can be attributed to small differences in the initial Q -profile (see Fig. 4). For example, models A_1 and A_5 have $Q = 1.2$ and $Q = 1.4$, respectively, at $2.5R_d$. The stellar disk of A_5 is therefore slightly warmer, and it grows the $m = 2$ component more slowly than the A_1 disk. However, once the initial phase is over, A_5 grows a stronger bar than A_1 . The same dependence on Q holds for the type B models: during the initial growth phase, low- Q models tend to grow the $m = 2$ component faster than their relatively high- Q counterparts. The models

with very similar initial condition also tend to evolve similarly, e.g., B_3 and B_4 , compare table 1 and Fig. 4. In the final phase (after about 3. Gyr), the models show wide variations in the strength of A_2/A_0 . Fig. 5 shows the morphology of all 15 models at the end of ~ 3.5 Gyr - some are clearly barred and some not. Slight initial variations in Q values alone seem to be difficult in providing an explanation for such wide variation in A_2/A_0 in the final phase. Other physical process and/or initial parameters must be involved, as discussed in the following sections.

The models that eventually grew a bar at about 1 Gyr (see Fig. 5), had their amplitudes remain roughly constant for the next several rotation times (see Fig. 4). Normally, one would expect a bar to grow in amplitude via continuously transferring angular momentum to the surrounding dark matter halo (Tremaine & Weinberg 1984; Weinberg 1985; Hernquist & Weinberg 1992; Debattista & Sellwood 2000; Athanassoula 2002; Sellwood & Debattista 2006; Dubinski et al. 2009; Saha & Naab 2013). Note, the inner regions of these models are dominated by the disk and bulge, with dark matter contributing little to the inner rotation curves; basically, these models are maximum-disk models. The transfer of angular momentum depends primarily on the degree of non-axisymmetry (here, the bar strength) and whether there are adequate halo and disk particles around (Weinberg & Katz 2007a,b) to take away the angular momentum. A part of this angular momentum from the inner region can be transferred to the outer disk and another part of it to the halo and bulge. We

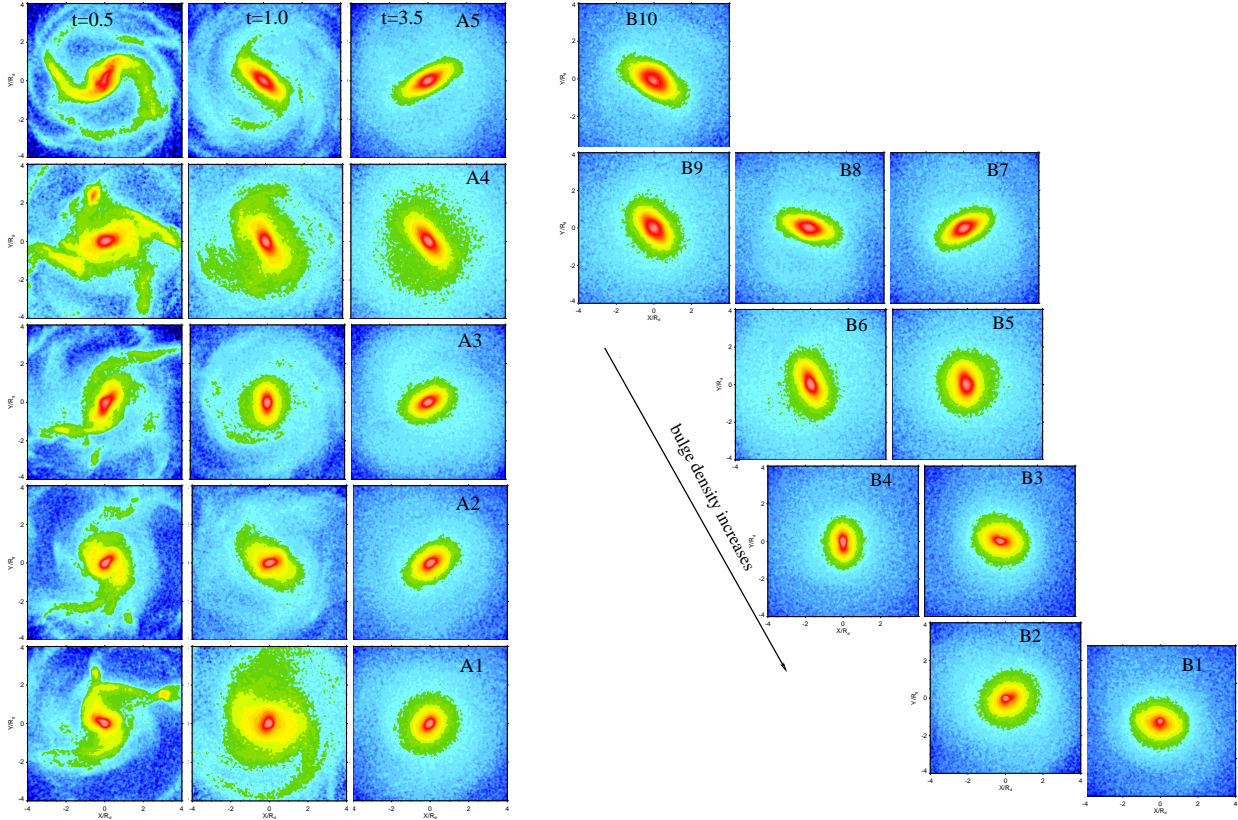


FIG. 5.— Left panels: face-on surface density maps and their time sequence for type-A models. Model with highest density CIB in A-series (e.g., A_1) has no bar at the end of 3.5 Gyr. From upper panels to lower ones, the bulge density increases, making it difficult to grow bar at the highest density. Right panels: Same but for type B model galaxies at $t = 3.5$ Gyr. Models are arranged according to their bulge density.

calculated the radial angular momentum profiles at different times and found that when the inner disk loses, a fraction of it goes to the outer parts and the dominant component goes to the dark halo.

Fig. 6 illustrates the total angular momentum exchange between the full disk, bulge, and dark matter halo in models A_1 and A_5 . In model A_1 (red curves), the dark matter halo absorbs angular momentum from the disk for an initial period of ~ 0.5 Gyr and then saturates

with $d(\Delta L_z)/dt = 0$. Consequently, the disk of A_1 did not grow a bar. On the other hand, in model A_5 (blue curves), the dark matter halo gains angular momentum continuously and thereby facilitates in growing the bar (see Fig. 5). Since the bulge is modelled with a distribution function $f(E)$, i.e., a function of energy only, it always gains a small fraction of angular momentum (e.g., Saha et al. 2012).

3.1. ILR effect

In the wave-mechanics picture, a stellar bar can be thought of as a standing wave mode - made by the linear superposition of a set of leading and trailing waves. Such a wave could grow via swing-amplification as proposed by Toomre (1981) for density waves. The amplification of the waves depends on the corotation resonance (CR) - which plays an important role in galactic dynamics. A CR essentially divides the whole galaxy into two dynamically distinct parts - the region inside CR having negative energy and angular momentum density in the wave and that outside having positive energy and angular momentum in the wave. So if a wave mode loses energy and angular momentum inside CR, it will grow. An wave incident on the CR will be partially reflected and a part will be transmitted which will carry positive energy (if coming from the inward direction) - then for the conservation of energy, the reflected wave from CR will be with higher (more negative) energy (or amplitude). This inward travelling (trailing) waves can be reflected in the center if there no strong inner Lindblad resonance

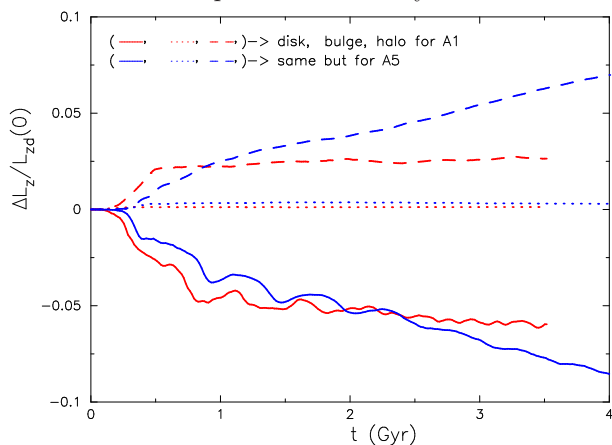


FIG. 6.— Angular momentum exchange between the stellar disk and dark matter halo for models A_1 (red curves) and A_5 (blue curves). $L_{zd}(0)$ is the z-component of the disk angular momentum at $t=0$. The gain of angular momentum by the dark halo of A_1 saturates after 0.5 Gyr.

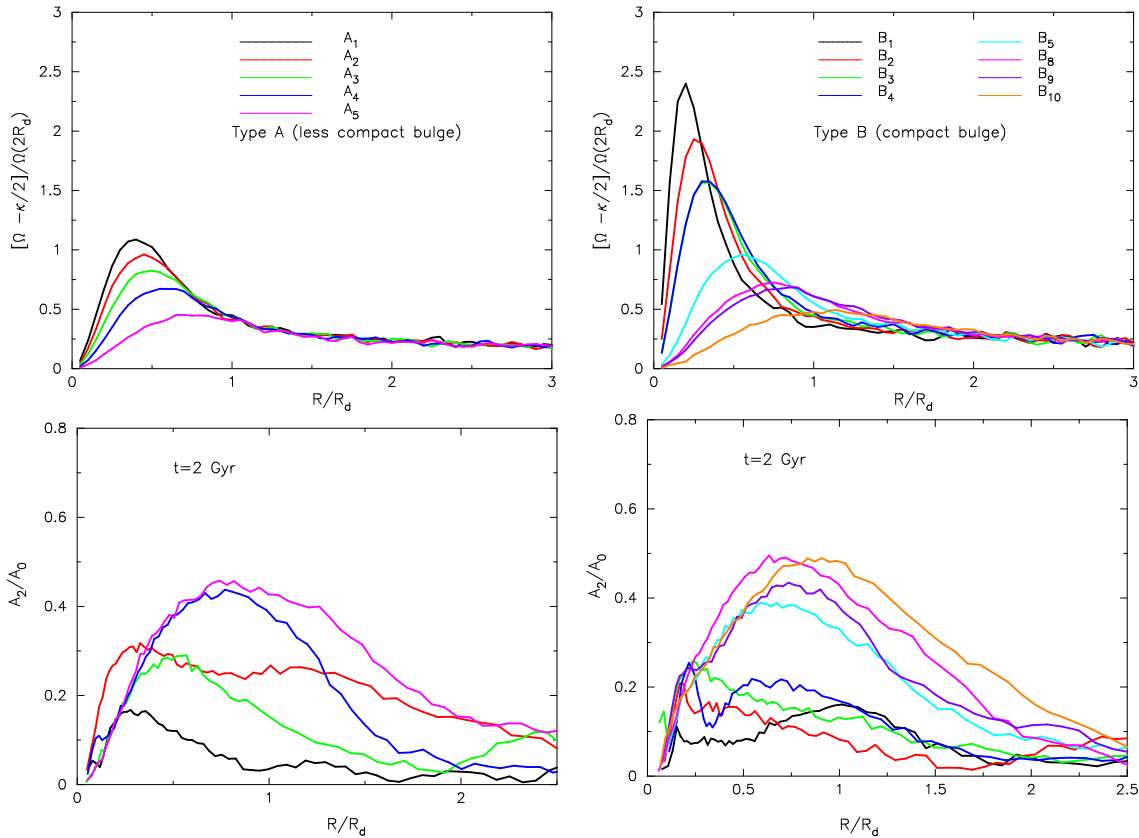


FIG. 7.— Left panels: initial ILR curves (upper) and radial profile of A_2/A_0 (lower) for type A models. Right panels: same as the left panels but for type B

(ILR) to absorb the waves (Lynden-Bell & Kalnajs 1972) - acting as a negative feedback. A centrally concentrated bulge produces a strong ILR and prevents the feedback loop, hindering the bar growth (Sellwood & Evans 2001).

The strength of the ILR, defined as $[\Omega - \kappa/2]/\Omega(2R_d)$ (Saha & Elmegreen 2016), increases as the ClBs become more and more compact and the peak of the ILR curve shifts inwards (see the upper panels of Fig. 7). For the most compact ClB, B_1 , the ILR peak lies within $\sim 0.1R_d$. The differences in the ILR curves are entirely the result of the different initial bulge sizes and masses, be-

cause the initial disks and dark halo parameters are kept nearly same in each model - ideally suited for isolating the impact of bulges alone. In the lower panels of Fig. 7, we show the radial variation of A_2/A_0 . For both types of bulges, the peak location of A_2/A_0 occurs at smaller radii as the ILR peak shifts inward. At the same time, the strength (maximum value of A_2/A_0) also decreases.

In Fig. 8, we show that during the initial phase of disk evolution, the model A_5 grows a bar such that it avoids a low pattern speed which would give it an ILR i.e., the early bar in A_5 starts with a pattern speed $\Omega_B > \max[\Omega - \kappa/2]$. Later, the bar grows via losing angular momentum to the halo which in turn decreases the pattern speed. At $t = 3.5$ Gyr, the pattern speed reduces to $\Omega_B = 21.9 \text{ km s}^{-1} \text{ kpc}^{-1}$ and it intersects the $\Omega - \kappa/2$ curve at two radii - producing two ILRs, allowing the formation of x_2 orbits in between the two radii. This holds true for other models forming a bar in our simulations. Both Fig. 7 and Fig. 8 thus brings out two aspects of bar formation -

First: The final bar amplitude is found to be lower for models with higher initial ILR strength; for the most compact ClB, a bar is barely visible even after several rotation times.

Second: The radius corresponding to the peak in the initial ILR curve is about the same as the radius of the maximum bar amplitude (i.e., peak of A_2/A_0 , see Fig. 7). Thus the more centrally concentrated bulges, which have shorter and stronger ILRs, force their incipient bars to be short and fast-rotating also, making them difficult to observe or short-lived.

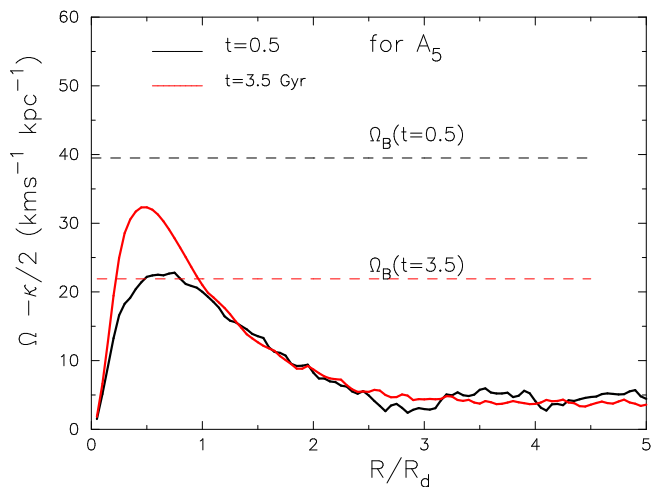


FIG. 8.— ILR curve plotted as function of radius for A_5 . Two horizontal lines mark the bar pattern speed (Ω_B) at $t = 0.5$ and 3.5 Gyr.

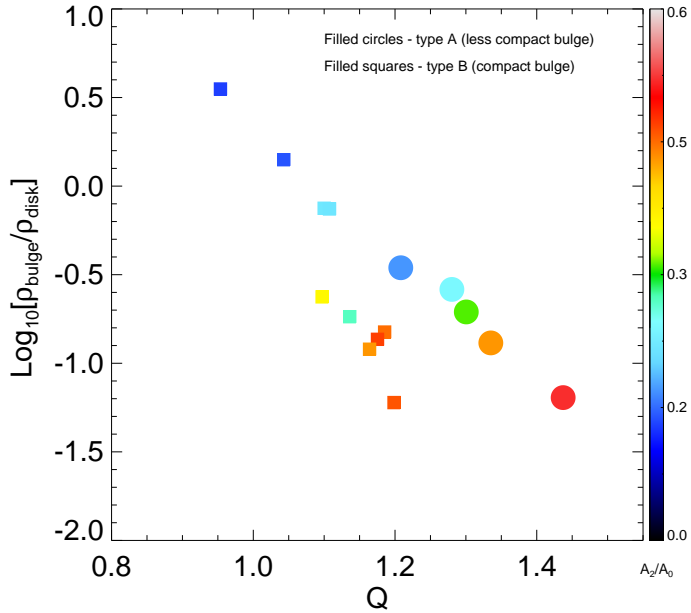


FIG. 9.— Bar evolution on the $Q - \rho_{bulge}$ plane. The Q values are taken at $2.5R_d$; both Q and ρ_{bulge}/ρ_{disk} are computed at $t=0$. Color scale is determined by the max of A_2/A_0 at 3.5 Gyr.

From an orbital point of view, a centrally concentrated CIB (e.g., model B_1) might also have the effect of preventing the x_1 orbit families from developing in the first place. Any star on a highly eccentric x_1 orbit would pass close to the centre and be knocked to a different orbit, which would generally be more circular (Pfenniger & Norman 1990; Hasan et al. 1993). From both points of view, a strong ILR would be necessary to prevent a bar from growing and we show that this is possible in the presence of a compact bulge.

3.2. Bar strength vs bulge density and Toomre Q

Fig. 9 summarizes how the growth of a bar depends on the the initial Toomre Q and the normalized average bulge density. In other words, this plot aims at understanding the relative role of the initial Toomre Q and ρ_{bulge}/ρ_{disk} in deciding whether a given model will evolve into a barred or unbarred one. Although there is no clear boundary between barred and unbarred ones in terms of A_2/A_0 values, for all practical purposes, a bar is clearly visible only when A_2/A_0 exceeds ~ 0.2 (Saha & Naab 2013). If we consider this (i.e., $A_2/A_0 = 0.2$) as the boundary between barred and unbarred galaxies (operational definition), an interesting outcome arises from this figure. For type B models, we see that only those models with $\rho_{bulge}/\rho_{disk} > 1$ evolve into clear unbarred galaxies e.g., B_1 , B_2 . Models B_3 and B_4 are both just above the marginal case which is similar to galaxies with intermediate bar types, such as SAB's with oval distortions (see the right panel of Fig. 5). Examining all our simulation sample, it turns out that all those model galaxies evolved to become unbarred for which the initial $\rho_{bulge}/\rho_{disk} > 1/\sqrt{10}$ even though they had the necessary range of Q values. In other words, a bar would preferentially form in an extended bulge than in a com-

compact bulge, given the same disk and halo. Overall, there is a clear trend that as ρ_{bulge}/ρ_{disk} increases, the bar strength decreases although the disk may have Toomre Q favourable for the bar formation.

4. DISSECTION OF MODELS A_1 AND A_5

The aim of this section is to carry out a detailed investigation on how the stellar disk of the model A_5 eventually becomes unstable to bar formation while model A_1 remains stable.

4.1. Early morphological evolution

In this section, we describe the early evolution of the star particles in models A_1 and A_5 ; both belong to Type A bulges - A_1 hosts a compact, dense bulge while A_5 has a less compact bulge (see Tabel 1). In Fig. 10 and Fig. 11, we show the early morphological evolution of these two models. Since the disk of A_1 is slightly colder than A_5 (see Fig. 4), it develops spiral arms faster (within a rotation time-scale) than A_5 . The spiral arms reach their peak strength ($A_2/A_0 \sim 0.6$) within about 250 Myr and then break down due to non-linear processes, forming large stellar clumps which migrate to the central region - eventually leaving the disk in a state with negligible non-axisymmetric features. Whereas, model A_5 being slightly warmer, grows spiral arms rather slowly and reaches its peak value ($A_2/A_0 \sim 0.6$) around 500 Myr. Beyond this point of time, the spiral arms do not sustain, but they decay due to the radial heating they produce in the disk. So the basic differences in the early evolutionary phases of models A_1 and A_5 are as follows. In model A_1 , spiral arms grow quickly and fragment into pieces because the initial disk is slightly colder, forming stellar clumps and dissolving. Whereas, in model A_5 , the spiral arms grow more slowly and eventually decay due to the slow radial heating they produce through scattering. In the section below, we use these observations to connect with detailed physical processes involved.

4.2. Ostriker-Peebles criteria for bar formation

Based on the stability analysis of the Maclaurin disks (see, Binney & Tremaine 1987, and references therein) and collisionless N-body simulations of galaxies, it was shown by Ostriker & Peebles (1973) that a stellar disk would go bar unstable if the ratio of the rotational kinetic energy T_{rot} to potential energy W i.e., $T_{rot}/|W|$ exceeds a critical value of 0.14 ± 0.003 . According to Lake (1983), not only the disk, stellar bulges with $V/\sigma \sim 0.8$ might also suffer a bar instability. We use the Ostriker-Peebles criteria to understand whether a model from our simulation sample evolves to become barred galaxy. Assuming the virial theorem holds for successive snapshots in an N-body simulation, the above mentioned criterion can be translated in terms of the rotational and random kinetic energy alone. From each snapshot, we compute the kinetic energy associated with the random and mean motion as follows:

The random kinetic energy is given by

$$\Pi(r) = \Pi_R(r) + \Pi_\varphi(r) + \Pi_z(r), \quad (4)$$

where each component of the random kinetic energy is calculated as, following Binney & Tremaine (1987):

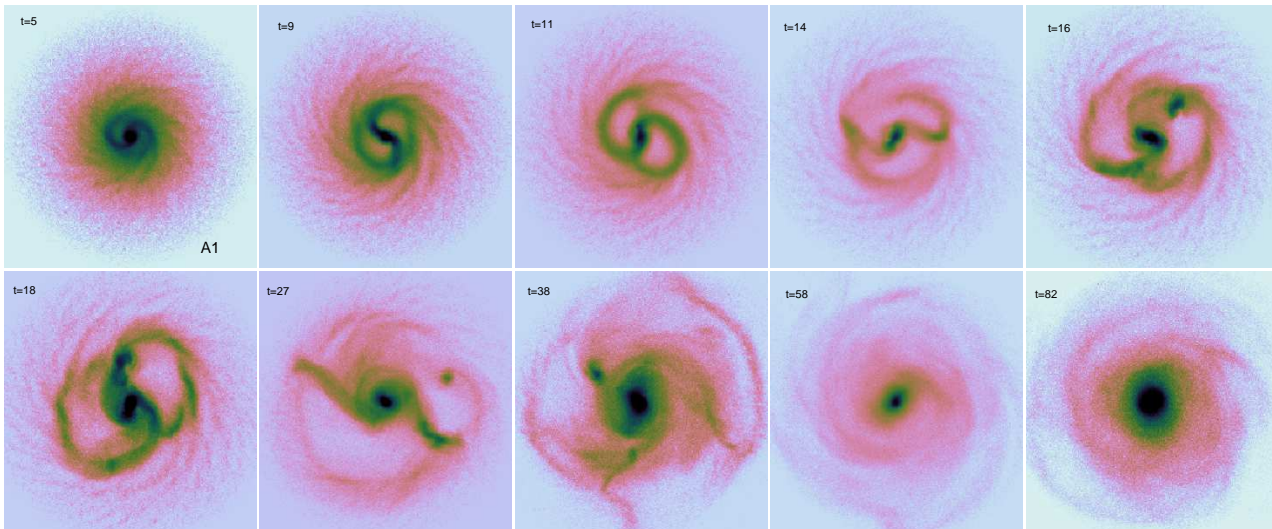


FIG. 10.— Density maps: close look at the first Gyr of evolution for A_1 .

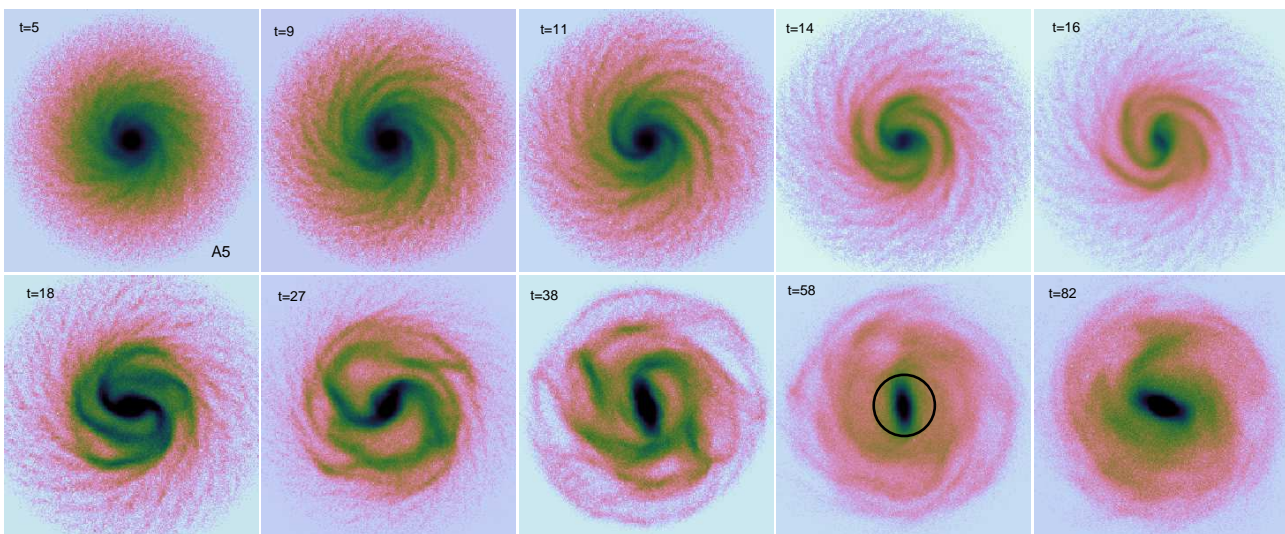


FIG. 11.— Density maps: close look at the first Gyr of evolution for A_5 . The circle encompassing the bar at $t = 58$ has a radius of $R_{bar} = 1.5R_d$.

$$\Pi_j(r) = \sum_{i=1}^{N_r} m(i) \sigma_j(i)^2 \quad (5)$$

In the above equation, $j = R, \varphi, z$; σ_j is the j^{th} component of the velocity dispersion, and N_r is the number of particles, each with mass m in a given circular annuli, $r, r + dr$ with dr fixed throughout the calculation. We have also calculated the mean kinetic energy of the system in the given annuli.

$$T_j(r) = \sum_{i=1}^{N_r} \frac{1}{2} m(i) \langle v_j \rangle^2, \quad (6)$$

where $\langle v_j \rangle$ is the j^{th} component of the mean velocity of a particle. Similar to equation above, we calculate the total mean kinetic energy associated with the annuli:

$$T_{mean}(r) = T_R(r) + T_\varphi(r) + T_z(r). \quad (7)$$

We have verified that the total mean kinetic energy is essentially the rotational kinetic energy. As the galaxy evolves, there are local variation or migrations which tend to contribute to the radial and vertical kinetic energy - but the galaxy as a whole has no mean motion either in the radial or vertical direction. This allows one to essentially replace T_{mean} by $T_\varphi = T_{rot}$. Then following the tensor-virial theorem in a steady state (Binney & Tremaine 1987), we can write (using the trace of the kinetic and potential energy tensors)

$$\Pi + 2T_{rot} + W = 0. \quad (8)$$

Then using the above equation, the Ostriker-Peebles criterion for bar instability becomes,

$$\frac{T_{rot}}{|\Pi + 2T_{rot}|} > 0.14, \quad (9)$$

or

$$\Pi/T_{rot} + 2 < 7.14 \Rightarrow \Pi/T_{rot} < 5.14 \quad (10)$$

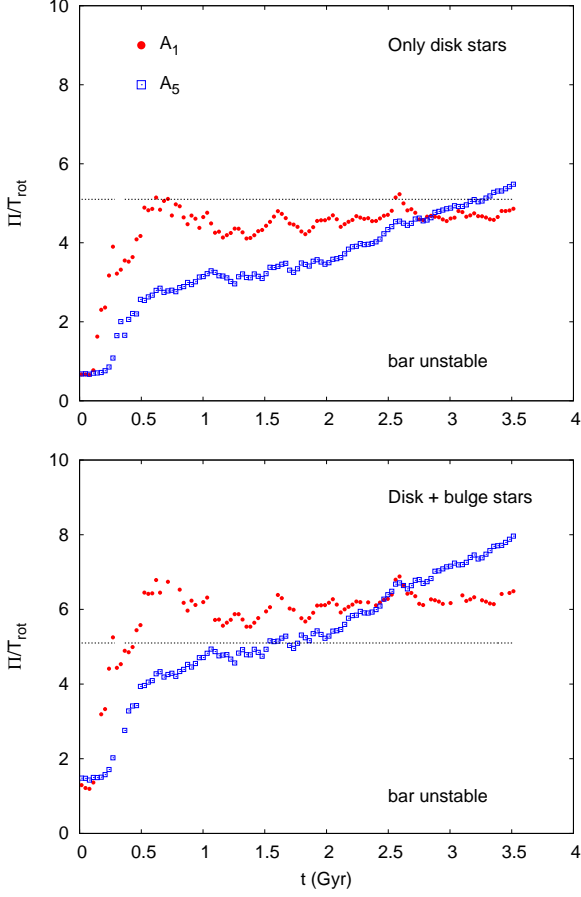


FIG. 12.— Ostriker-Peebles criteria for the stellar disks of models A_1 and A_5 . Upper: Only disk stars are included in the calculation. Lower: Disk plus bulge stars for the same. Model A_5 forms a bar and A_1 does not.

In other words, if $\Pi/T_{rot} < 5.14$, then a stellar disk becomes unstable to bar formation; Π denotes the random kinetic energy of the stars and T_{rot} is the kinetic energy associated with the rotational motion. We compute these quantities for each of the snapshots in our simulation using the above equations.

In Fig. 12, we show the time evolution of Π/T_{rot} for the two cases: stellar disk alone and stellar disk plus bulge. If the bulge stars are excluded from the computation, both of the cold stellar disks would have formed a bar, as also suggested by the initial value of $\Pi/T_{rot} \sim 0.37$, see the upper panel of Fig. 12. By adding the bulges to our calculation, the $\Pi/T_{rot}(t=0)$ increases to ~ 1.3 and ~ 1.7 for A_1 and A_5 respectively. Although these values have increased by a factor of 4–5, they are still less than 5.14 – ensuring that both models qualify for bar-instability according to Ostriker-Peebles criteria. But when we follow the subsequent evolution of these two models, only A_5 makes a bar at the end. Clearly, the final fate of a galaxy model is not entirely decided by the initial value of Π/T_{rot} .

4.3. Energy and Angular momentum budget

Here, we investigate the energy and angular momentum budget in the central $1.5R_d$ region (which encompass the bar that grows in A_5) of both of these galaxies

in detail. For each of the annuli/rings of fixed size (as mentioned above), we calculate the angular momentum as

$$L_z(r) = \sum_{i=1}^{N_r} m(i) \times [x(i)v_y(i) - y(i)v_x(i)], \quad (11)$$

Following Eq.5, we compute the random component of the kinetic energy associated with radial motions within the bar radius, $R_{bar} = 1.5R_d$, and this is repeated for every snapshot for both models. The upper panel of Fig. 13 shows the time variation of radial kinetic energy (Π_r) of the disk stars and the right panel shows their corresponding angular momentum. In A_1 , Π_r increases initially more rapidly than in A_5 . Such a rapid increase in heating is caused by the coalescence of two giant clump-like structures formed as a result of non-linear fragmentation of the spiral arms in the central region, at around $t = 0.25$ Gyr (see Fig. 10). Note that at this time, the radial kinetic energy in A_1 has increased roughly by a factor of 2 compared to that in A_5 . The coalescence of the two clumps in the central region of A_1 results in a sudden decrease in the angular momentum (right panel of Fig. 13). However, soon after, its angular momentum settles down to a fixed fraction ($\sim 12\%$) of the disk’s ini-

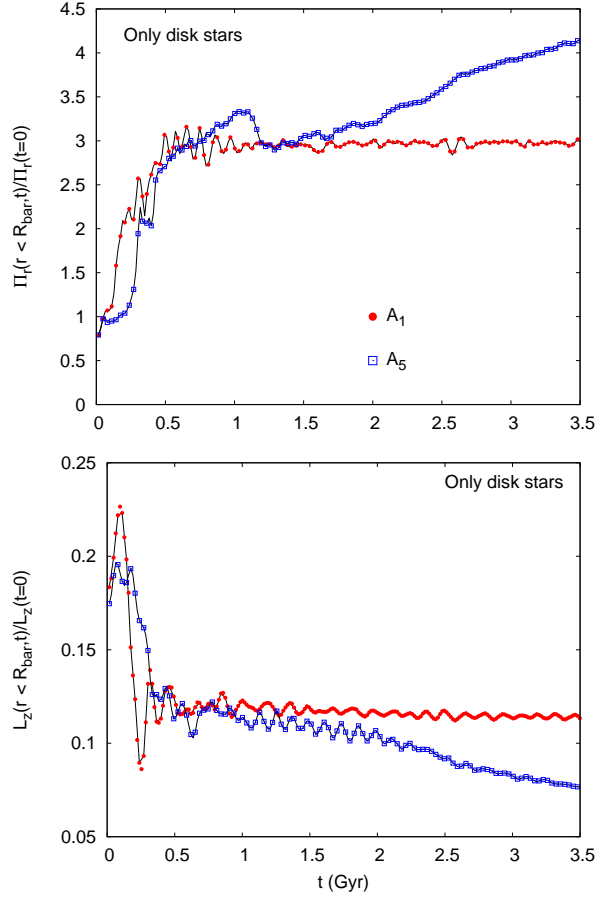


FIG. 13.— Upper: Time variation of the radial random kinetic energy of the stellar disk within bar radius for models A_1 (remained unbarred) and A_5 (became barred). Lower: Fraction of the disk total angular momentum calculated within the bar radius for both models.

tial angular momentum. During the subsequent phase of evolution, model A_1 does not undergo any major change; both radial kinetic energy and z-component of angular momentum stay nearly constant. Whereas in model A_5 , the inner stellar disk steadily loses angular momentum as would be expected for a disk that is growing a bar. The bar facilitates a steady loss of angular momentum from the inner disk accompanied by a steady increase in the radial kinetic energy (blue points in Fig. 13).

To summarise, in an isolated galaxy under virial equilibrium, a rapid (or non-adiabatic) loss of angular momentum is also accompanied by a non-adiabatic heating of the inner disk. As a result, orbital structure in the inner region has very little time to respond to such rapid non-adiabatic change in the disk angular momentum. This is probably causing the prevention of a bar in model A_1 . In other words, *the key to “not forming a bar” is to find a way such that the central part of the disk undergoes a sudden loss of angular momentum associated with simultaneous heating to a high degree.* This can be achieved in a galaxy model having a cold stellar disk and a compact bulge whose average density is greater than or comparable to the disk density within the bulge half-mass radius.

5. DISCUSSION AND CONCLUSIONS

The models A_1 , B_1 and B_2 have the most compact CLBs and they all evolve into galaxies with final $A_2/A_0 < 0.2$. Stronger $m = 2$ modes grow in models with more extended bulges of the same mass, i.e., lower density bulges. The orbits of the bulge stars are themselves hot thermal orbits and not circular, and that what is important for bar formation in the disk is the cold orbits of the sub-component of the “bulge-region” stars that is in the disk. Additionally, a hotter bulge is not easily deformed by perturbations in the disk, it is non-reactive and therefore disk perturbations can not amplify very much and grow into a disk bar. The bar needs x_1 orbits to reinforce it, and when the bar is initially weak, its pattern speed cannot be lower than the peak in $\Omega - \kappa/2$ because then x_2 orbits would form between the two ILR radii. Thus seed bars may come and go repeatedly at high angular frequency and small radius when the ILR peak is large, but such tiny bars are not typically classified as barred galaxies.

Our simulations are pure collisionless in nature, i.e., without any dissipative component such as cold gas. The presence of a gas component in N-body simulations of disk galaxies is known to contribute to the weakening of the already-present bar (Berentzen et al. 1998; Athanassoula et al. 2013). Added to this are the central mass concentrations (CMC) and super-massive black holes (SMBH) at the galactic centre which have a destructive effect on the galactic bar (Hasan et al. 1993; Bournaud et al. 2005; Hozumi & Hernquist 2005). Nonetheless as shown by Athanassoula et al. (2005), a bar is hard to destroy completely either by CMCs or SMBHs.

The main results from our work are as follows:

1. Our simulations, in essence, show how a cold stellar disk that is prone to bar instability prevents a bar from forming in the presence of a compact and highly dense classical bulge.
2. Based on pure stellar dynamical effects, we suggest that the recipe to prevent frequent bar formation in simulations is to let the central few kpc region of the stellar disk undergo a non-adiabatic (rapid) loss of angular momentum accompanied by a simultaneous rise in the radial kinetic energy.
3. The analyses from our simulations suggest that model galaxies that prevent bar formation and remained completely unbarred at later stages of evolution, had their initial bulge densities greater than or comparable to the disk density measured within the bulge half-mass radii.
4. The bars that formed in our simulations during the early phase of the evolution had their pattern speed always greater than the maximum of $\Omega - \kappa/2$, i.e., the early bars avoided the ILR. The barred galaxies also had a low ratio of random energy to rotational energy, less than ~ 5.14 , for over a Gyr initially while the non-barred galaxy models reached a high ratio fairly early, in less than half a Gyr. The prolonged period of relatively low random energy allowed the bar to form over several rotation periods.

ACKNOWLEDGEMENT

The numerical simulations were carried out at the IUCAA HPC cluster. The authors thank the anonymous referee for useful comments.

REFERENCES

- Athanassoula, E. 2002, ApJ, 569, L83
— 2003, MNRAS, 341, 1179
Athanassoula, E., Lambert, J. C., & Dehnen, W. 2005, MNRAS, 363, 496
Athanassoula, E., Machado, R. E. G., & Rodionov, S. A. 2013, MNRAS, 429, 1949
Athanassoula, E., & Misiriotis, A. 2002, MNRAS, 330, 35
Barazza, F. D., Jogee, S., & Marinova, I. 2008, ApJ, 675, 1194
Barnes, J. E., & Hernquist, L. E. 1991, ApJ, 370, L65
Berentzen, I., Heller, C. H., Shlosman, I., & Fricke, K. J. 1998, MNRAS, 300, 49
Binney, J., & Tremaine, S. 1987, Galactic dynamics, ed. Binney, J. & Tremaine, S.
Bournaud, F., & Combes, F. 2002, A&A, 392, 83
Bournaud, F., Combes, F., & Semelin, B. 2005, MNRAS, 364, L18
Ceverino, D., & Klypin, A. 2007, MNRAS, 379, 1155
Combes, F., & Sanders, R. H. 1981, A&A, 96, 164
Debattista, V. P., & Sellwood, J. A. 1998, ApJ, 493, L5
— 2000, ApJ, 543, 704
Dubinski, J., Berentzen, I., & Shlosman, I. 2009, ApJ, 697, 293
Elmegreen, D. M., Sundin, M., Sundelius, B., & Elmegreen, B. 1991, A&A, 244, 52
Eskridge, P. B., Frogel, J. A., Pogge, R. W., et al. 2000, AJ, 119, 536
Evans, N. W. 1993, MNRAS, 260, 191
Gerin, M., Combes, F., & Athanassoula, E. 1990, A&A, 230, 37
Goldreich, P., & Tremaine, S. 1979, ApJ, 233, 857
Grosbøl, P., Patsis, P. A., & Pompei, E. 2004, A&A, 423, 849
Hasan, H., Pfenniger, D., & Norman, C. 1993, ApJ, 409, 91
Hernquist, L., & Weinberg, M. D. 1992, ApJ, 400, 80
Hohl, F. 1971, ApJ, 168, 343
Holley-Bockelmann, K., Weinberg, M., & Katz, N. 2005, MNRAS, 363, 991
Hozumi, S., & Hernquist, L. 2005, PASJ, 57, 719
King, I. R. 1966, AJ, 71, 64
Kuijken, K., & Dubinski, J. 1995, MNRAS, 277, 1341
Lake, G. 1983, ApJ, 264, 408
Lynden-Bell, D., & Kalnajs, A. J. 1972, MNRAS, 157, 1

- McMillan, P. J., & Dehnen, W. 2007, *MNRAS*, 378, 541
- Menéndez-Delmestre, K., Sheth, K., Schinnerer, E., Jarrett, T. H., & Scoville, N. Z. 2007, *ApJ*, 657, 790
- Miller, R. H., Prendergast, K. H., & Quirk, W. J. 1970, *ApJ*, 161, 903
- Miwa, T., & Noguchi, M. 1998, *ApJ*, 499, 149
- Noguchi, M. 1987, *MNRAS*, 228, 635
- Ostriker, J. P., & Peebles, P. J. E. 1973, *ApJ*, 186, 467
- Pfenniger, D., & Norman, C. 1990, *ApJ*, 363, 391
- Polyachenko, E. V. 2013, *Astronomy Letters*, 39, 72
- Romano-Díaz, E., Shlosman, I., Heller, C., & Hoffman, Y. 2008, *ApJ*, 687, L13
- Saha, K., & Elmegreen, B. 2016, *ApJ*, 826, L21
- Saha, K., Martínez-Valpuesta, I., & Gerhard, O. 2012, *MNRAS*, 421, 333
- Saha, K., & Naab, T. 2013, *MNRAS*, 434, 1287
- Saha, K., Tseng, Y., & Taam, R. E. 2010, *ApJ*, 721, 1878
- Sellwood, J. A., & Debattista, V. P. 2006, *ApJ*, 639, 868
- Sellwood, J. A., & Evans, N. W. 2001, *ApJ*, 546, 176
- Sellwood, J. A., & Wilkinson, A. 1993, *Reports on Progress in Physics*, 56, 173
- Shen, J., & Sellwood, J. A. 2004, *ApJ*, 604, 614
- Sheth, K., Melbourne, J., Elmegreen, D. M., et al. 2012, *ApJ*, 758, 136
- Sheth, K., Elmegreen, D. M., Elmegreen, B. G., et al. 2008, *ApJ*, 675, 1141
- Springel, V., Yoshida, N., & White, S. D. M. 2001, *NewA*, 6, 79
- Toomre, A. 1964, *ApJ*, 139, 1217
- Toomre, A. 1981, in *Structure and Evolution of Normal Galaxies*, ed. S. M. Fall & D. Lynden-Bell, 111–136
- Tremaine, S., & Weinberg, M. D. 1984, *MNRAS*, 209, 729
- Weinberg, M. D. 1985, *MNRAS*, 213, 451
- Weinberg, M. D., & Katz, N. 2007a, *MNRAS*, 375, 425
- . 2007b, *MNRAS*, 375, 460